

# Array-based optical nanolithography using optically trapped microlenses

Euan McLeod and Craig B. Arnold

*Department of Mechanical & Aerospace Engineering  
Princeton University, Princeton, NJ*

[cbarnold@princeton.edu](mailto:cbarnold@princeton.edu)

**Abstract:** Current demands on optical nanolithography require the ability to rapidly and cost-effectively write arbitrary patterns over large areas with sub-diffraction limit feature sizes. The challenge in accomplishing this with arrays of near-field probes is maintaining equal separations between the substrate and each probe, even over non-planar substrates. Here we demonstrate array-based laser nanolithography where each probe is a microsphere capable of fabricating 100 nm structures using 355 nm light when self-positioned near a surface by Bessel beam optical trapping. We achieve both a feature size uniformity and relative positioning accuracy better than 15 nm, which agrees well with our model. Further improvements are possible using higher power and/or narrower Bessel beam optical traps.

© 2009 Optical Society of America

**OCIS codes:** 110.4235 (Nanolithography); 350.3390 (Laser materials processing); 350.4855 (Optical tweezers or optical manipulation)

---

## References and links

1. T. A. Nieminen, V. L. Y. Loke, A. B. Stilgoe, G. Knoner, A. M. Branczyk, N. R. Heckenberg, and H. Rubinsztein-Dunlop, "Optical tweezers computational toolbox," *J. Opt. A: Pure Appl. Opt.* **9**, S196–S203 (2007).
2. H. J. Munzer, M. Mosbacher, M. Bertsch, J. Zimmermann, P. Leiderer, and J. Boneberg, "Local field enhancement effects for nanostructuring of surfaces," *J. Microsc.* **202**, 129–135 (2001).
3. K. Pigmayer, R. Denk, and D. Bauerle, "Laser-induced surface patterning by means of microspheres," *Appl. Phys. Lett.* **80**, 4693–4695 (2002).
4. Z. B. Wang, M. H. Hong, B. S. Luk'yanchuk, Y. Lin, Q. F. Wang, and T. C. Chong, "Angle effect in laser nanopatterning with particle-mask," *J. Appl. Phys.* **96**, 6845–6850 (2004).
5. W. Guo, Z. B. Wang, L. Li, D. J. Whitehead, B. S. Luk'yanchuk, and Z. Liu, "Near-field laser parallel nanofabrication of arbitrary-shaped patterns," *Appl. Phys. Lett.* **90**, 243101 (2007).
6. R. M. Langford, P. M. Nellen, J. Gierak, and Y. Fu, "Focused ion beam micro- and nanoengineering," *MRS Bull.* **32**, 417–423 (2007).
7. A. Chimmalgi, C. P. Grigoropoulos, and K. Komvopoulos, "Surface nanostructuring by nano-femtosecond laser-assisted scanning force microscopy," *J. Appl. Phys.* **97**, 104319 (2005).
8. D. J. Hwang, A. Chimmalgi, and C. P. Grigoropoulos, "Ablation of thin metal films by short-pulsed lasers coupled through near-field scanning optical microscopy probes," *J. Appl. Phys.* **99**, 044905 (2006).
9. M. A. Case, G. McLendon, Y. Hu, T. K. Vanderlick, and G. Scoles, "Using nanografting to achieve directed assembly of de novo designed metalloproteins on gold," *Nano Lett.* **3**, 425–429 (2003).
10. Y. J. Chen, J. H. Hsu, and H. N. Lin, "Fabrication of metal nanowires by atomic force microscopy nanoscratching and lift-off process," *Nanotechnology* **16**, 1112–1115 (2005).
11. J. S. Hyun, J.-S. Moon, J.-H. Park, J. W. Kim, Y. D. Kim, and J.-H. Boo, "Fabrication of near-field optical probes using advanced functional thin films for mems and nems applications," *Mat. Sci. Eng. B-Solid* **149**, 292–298 (2008).
12. M. Lenczner and R. C. Smith, "A two-scale model for an array of afm's cantilever in the static case," *Math. Comput. Model.* **46**, 776–805 (2007).
13. F. Huo, Z. Zheng, G. Zheng, L. R. Giam, H. Zhang, and C. A. Mirkin, "Polymer pen lithography," *Science* **321**, 1658–1660 (2008).

14. J.-i. Kato, N. Takeyasu, Y. Adachi, H.-B. Sun, and S. Kawata, "Multiple-spot parallel processing for laser micro-nanofabrication," *Appl. Phys. Lett.* **86**, 044102 (2005).
15. Y. Lin, M. H. Hong, T. C. Chong, C. S. Lim, G. X. Chen, L. S. Tan, Z. B. Wang, and L. P. Shi, "Ultrafast-laser-induced parallel phase-change nanolithography," *Appl. Phys. Lett.* **89**, 041108 (2006).
16. E. McLeod and C. B. Arnold, "Subwavelength direct-write nanopatterning using optically trapped microspheres," *Nature Nanotech.* **3**, 413–417 (2008).
17. J. Durnin, "Exact solutions for nondiffracting beams. i. the scalar theory," *J. Opt. Soc. Am. A* **4**, 651–654 (1987).
18. D. McGloin and K. Dholakia, "Bessel beams: diffraction in a new light," *Contemp. Phys.* **46**, 15–28 (2005).
19. V. Garces-Chavez, D. McGloin, H. Melville, W. Sibbett, and K. Dholakia, "Simultaneous micromanipulation in multiple planes using a self-reconstructing light beam," *Nature* **419**, 145–147 (2002).
20. E. J. W. Verwey and J. T. G. Overbeek, *Theory of the Stability of Lyophobic Colloids* (Elsevier Publishing Company, Inc., 1948).
21. J. Y. Walz and D. C. Prieve, "Prediction and measurement of the optical trapping forces on a microscopic dielectric sphere," *Langmuir* **8**, 3073–3082 (1992).
22. D. G. Grier, "A revolution in optical manipulation," *Nature* **424**, 810–816 (2003).
23. M. Himmelbauer, E. Arenholz, D. Bauerle, and K. Schilcher, "Uv-laser-induced surface topology changes in polyimide," *Appl. Phys. A* **63**, 337–339 (1996).
24. K. Piglmayer, E. Arenholz, C. Ortwein, N. Arnold, and D. Bauerle, "Single-pulse ultraviolet laser-induced surface modification and ablation of polyimide," *Appl. Phys. Lett.* **73**, 847–849 (1998).
25. We have also performed this calculation using a more accurate Mie scattering model [1], however the error is less than 5% with our parameters and the added complexity obscures the physics behind the trapping.
26. Y. Harada and T. Asakura, "Radiation forces on a dielectric sphere in the rayleigh scattering regime," *Opt. Commun.* **124**, 529–541 (1996).
27. E. McLeod and C. B. Arnold, "3d positioning accuracy of bessel beam surface traps balanced by electrostatic double-layer repulsion," in preparation .

## 1. Introduction

Many areas of nanoscience and technology require the ability to draw arbitrary patterns with high throughput at the 100 nm scale and below. Self-assembly methods are highly parallel, but are not capable of producing arbitrary patterns [2, 3], although significant effort has been made in extending the types of patterns that can be generated [4, 5]. On the other end of the spectrum are probe-based techniques such as electron and focused ion beam lithography [6], high-fluence near-field scanning optical microscopy [7, 8], and "nano-scratching" or "nano-grafting" with AFM tips [9, 10]. These methods can draw arbitrary patterns, however parallelization for high throughput can be difficult. For electron and ion beam lithography techniques, this is due to the cost of the sources. For near-field scanning optical microscopy or atomic force microscopy, fabrication of many probe tips on the same device is required [11]. In addition, the geometry and configuration of the probe tips cannot be altered after fabrication, and it is difficult to ensure that all probe tips interact with the surface equally due to the coupling in the system [12]— a task which is especially hard on tilted or uneven surfaces. Being able to write features in parallel on a surface reduces fabrication time and therefore lowers the cost per area of nanostructured surfaces, as has been found with polymer pen lithography [13], and laser microlens array lithography [14, 15].

Here we present a major step forward in generating arbitrary nanopatterns: a parallel array implementation of optical trap assisted nanolithography (Fig. 1), which has previously been demonstrated with a single probe [16]. This technique uses two lasers for patterning. One continuous wave (CW) laser beam is converted into a Bessel beam [17, 18] and is used to optically trap a microsphere lens near a surface. The other laser is pulsed and is used to illuminate the trapped bead and surrounding surface. The energy of the pulsed laser is tuned so that the necessary fluence for material modification is only obtained directly beneath the microsphere because of focusing and near-field enhancement. Patterns are drawn by moving the substrate relative to the optical trap.

The Bessel beam trap is key to this technique because of its two-dimensional nature [19]. The long line focus and nondiffracting nature provide a constant radiation pressure on the mi-

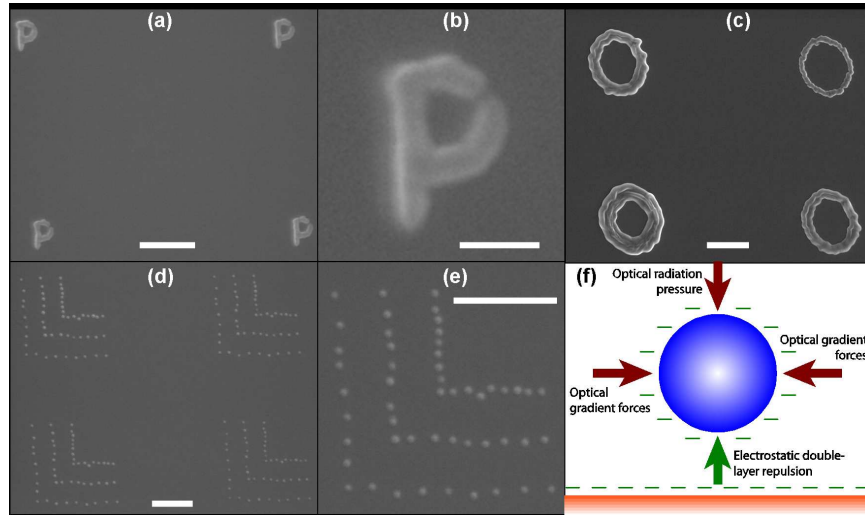


Fig. 1. Parallel nanolithography. (a) Four P's written using overlapping laser pulses with  $10 \text{ mJ/cm}^2$  incident fluence. (b) Overlaid image of the four P's in (a). (c) Four O's written using  $12 \text{ mJ/cm}^2$  fluence and a  $0.76 \mu\text{m}$  bead (upper-right), two  $2.0 \mu\text{m}$  beads, and a  $3.0 \mu\text{m}$  bead (lower-left). This illustrates the capability to simultaneously produce different line widths in an array. (d) Four test patterns of individual shots used to test positioning accuracy and feature size uniformity. The incident fluence is  $15 \text{ mJ/cm}^2$ . (e) The overlaid image of the four patterns in (d), illustrating the identical nature of the patterns. (f) Forces acting on the microsphere that maintain its position relative to the substrate. The balance between the electrostatic repulsion and the optical radiation pressure allows the sphere to maintain its position away from the surface without active control and feedback. All panels: The trapping power in each beam is  $140 \text{ mW}$ , the scale bar in (b) is  $500 \text{ nm}$ , all other scale bars are  $2 \mu\text{m}$  long, and unless noted the bead size is  $0.76 \mu\text{m}$ .

crossphere while maintaining constant in-plane trapping forces over an extended range in the direction normal to the surface [16]. The length of this region depends on the amount of demagnification and the properties of the Bessel beam used. For the experiment here, typical values are on the order of tens of microns. Contrary to conventional optical traps, the position of the microsphere relative to the surface is not determined by the three-dimensional location of the optical trap, but rather by the balance of the Bessel beam radiation pressure with the electrostatic double-layer repulsion [20, 21], which develops due to ionic groups on the surfaces (Fig. 1(f)). This provides a major benefit to the approach because particle-substrate separation distances are maintained without any complicated feedback or sensing mechanisms.

This self-positioning of the particle relative to the substrate is instrumental in enabling parallel processing because it eliminates any mechanical coupling between probes, allowing each bead to find its equilibrium spacing without perturbing the others. This facilitates the patterning of uneven or curved surfaces where the absolute elevation of each probe in the lab frame will change during patterning, yet the relative separations between each probe and the substrate will be held constant. With a single processing laser pulse, we illuminate multiple beads contained in individual traps. To create the array of traps, we simply split the trapping laser beam into four parallel beams to trap four beads at the same time. We do this using beam splitters (Fig. 2), but additional functionality can be achieved using diffractive optical elements or spatial light modulators [22]. Spheres of the same or different sizes may be used in the array to produce

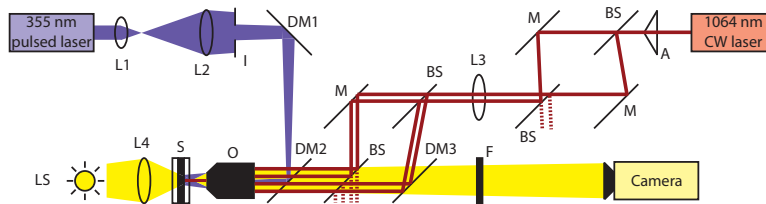


Fig. 2. Experimental setup. A: 178° Axicon. BS: 50/50 beam splitters for 1064 nm. DM1 & DM2: Dichroic mirrors designed to reflect 355 nm light. DM3: Dichroic mirror designed to reflect 1064 nm light. F: Short pass filter for blocking wavelengths above 800 nm. I: Iris. L1-L4: Converging lenses with respective focal lengths 50, 200, 200, and 25 mm. LS: Fiber light source. M: Silver mirrors. O: 60X microscope objective. S: Sample cell, mounted on an XYZ translation stage.

patterns with the same (Figs. 1 (a), (b), (d), and (e)) or varying feature sizes between patterns (Fig. 1(c)).

In addition to demonstrating the potential for high-throughput nanolithography, the array-based approach used here allows us to demonstrate the fundamental limitations on positional accuracy and feature size uniformity by quantitatively comparing the generated patterns, thereby eliminating any errors due to thermal drift, macroscopic mechanical vibrations, and imprecisions in the translation stage. The remaining sources of variation include Brownian motion, variations in bead size, trapping power fluctuations, nonuniformities in the spatial fluence distribution, and shot-to-shot energy variations in the pulsed laser. We identify the relative importance of these factors in forming patterns.

## 2. Experimental methods

The experimental setup is shown in Fig. 2. The model substrate we use is a 3  $\mu\text{m}$  thick polyimide film. This is prepared by spin coating polyimide solution (HD Microsystems PI2525) onto a glass coverslip at 500 rpm for 10 s and then 8000 rpm for 40 s. The coverslips are then baked at 150 °C for 30 min followed by 350 °C for 30 min in order to cure the film.

Microspheres with a diameter of 0.76  $\mu\text{m}$  are obtained commercially in aqueous solution at a concentration of 9.6% by volume (Bangs Labs PS03N). This solution is then diluted by a factor of 1:750 so that extraneous beads do not typically enter the processing region, but it is still possible to find beads when scanning a larger area of the substrate. A 20  $\mu\text{L}$  drop of bead solution is placed on the polyimide coverslip. A piece of double-sided tape (Winmore, 90  $\mu\text{m}$  thick) with an interior region removed is placed around the droplet, forming a gasket. An uncoated coverslip is placed on top, completing the sample cell. The cell is mounted on an XYZ translation stage (ThorLabs MAX301), where the X, Y, and Z axes have manual coarse control and the X and Y axes have fine computer control with 5 nm resolution. After patterning, the sample cell is disassembled by soaking with ethanol and separating the tape from the coverslip using tweezers.

A 60X microscope objective (Edmund Optics DIN, NA = 0.85) is used in conjunction with a CMOS camera (Edmund Optics EO-5012C) to align and observe the experiment. The distance between the objective and the camera is 380 mm. Illumination is performed in transmission mode using a fiber light source (AmScope HL-250-A) focused using a 25 mm lens. A removable 850 nm short pass filter may be placed in front of the camera to block out any of the 1064 nm trapping laser beam that is reflected off of the surface.

To trap the microspheres, we use a 1064 nm laser (Spectra-Physics YHP40-106Q) run in

CW mode with output powers up to 7 W. The beam is passed through an axicon with  $178^\circ$  cone angle to generate a Bessel beam. This beam is then split into four parallel beams by passing it through two misaligned Mach-Zender interferometers. The first interferometer splits the beam horizontally into two parallel beams, while the second splits the beams vertically. The Bessel beam emerging from the axicon needs to be reduced in size to make it appropriate for trapping the  $0.76 \mu\text{m}$  spheres used in this experiment. This reduction is done using a telescope, where the first lens is a 200 mm converging lens placed between the two interferometers, and the second lens is the 60X microscope objective described above whose effective focal length is approximately 1.5 mm. This reduction produces a Bessel beam whose central lobe is 900 nm in radius, when measured in water. With the laser operating at 7 W total output power, each Bessel beam carries approximately 150 mW after passing through the objective. With approximately 8 rings in each Bessel beam in the focal plane, this results in up to 15 mW of power passing through the central lobe of the beam. The four beams are aligned in a rectangular configuration, with the distance between the beams being  $9 \mu\text{m}$  horizontally and  $6 \mu\text{m}$  vertically.

The processing laser is a pulsed 355 nm laser (Coherent Avia) with 15 ns pulse length. We used pulse energies in the range of 150 nJ to 8  $\mu\text{J}$ . The beam is then enlarged using a 50 mm lens followed by a 200 mm lens at a distance of 370 mm to make the beam converging so that it will not be truncated when entering the back aperture of the microscope objective. An adjustable iris is placed after this lens. The distance between the iris and microscope objective is the same as the distance between the camera and the microscope objective so that the iris is imaged onto the substrate when in focus. Hence, the iris is used to set the area of the processing laser beam without changing the fluence. The damage threshold for the polyimide film (without microsphere enhancement) was found to be  $55 \text{ mJ}/\text{cm}^2$ , in close agreement with previous findings [23, 24].

Beads are trapped by manually moving the stage until a bead is found and aligned with a trap location. Once four beads are trapped, the processing is performed using computer interface (Matlab) to control both lasers and the motion of the stage. The relative positioning accuracy of the technique is quantified by drawing a test pattern of discrete dots (see Figs. 1(c) and (d)). Such patterns are drawn at varying laser fluences and varying trap powers. Continuous patterns can also be generated using overlapping shots, as shown in Figs. 1(a) and (b).

The pattern quality is analyzed by taking SEM images of the array patterns, after sputter-coating the polyimide with 3.5 nm of Iridium. These images are acquired at 6500X magnification with a resolution of  $2576 \times 1936$ , resulting in a pixel size of 6.72 nm.

Once the images are captured, the locations and sizes of all spots in each image are determined (see appendix) and statistically characterized in order to evaluate the positioning accuracy and repeatability of the technique. The location of spot  $s$  in quadrant  $q$  is denoted  $(x_{q,s}, y_{q,s})$ , and its radius is denoted  $a_{q,s}$ . The statistical parameters that are calculated from this data are shown in Table 1.

### 3. Positioning accuracy model

Before presenting the experimental results, we first predict the transverse positioning error  $\langle r \rangle$  by calculating the Brownian and optical trapping forces. For particles whose radius  $R$  is less than the wavelength of light  $\lambda$ , Rayleigh scattering calculations can be used [25], and the optical gradient force on a particle is given by [26]

$$F(r) = \frac{2\pi n_m R^3}{c} \left( \frac{m^2 - 1}{m^2 + 2} \right) \nabla I(r), \quad (1)$$

where  $n_m$  is the refractive index of the surrounding medium,  $c$  is the speed of light in vacuum,  $m$  is the ratio of the refractive index of the particle to the surrounding refractive index, and  $I(r)$

Table 1. Statistical parameters.

symbol	description	formula
$\bar{a}$	Mean spot size	$\frac{1}{4S} \sum_{q=1}^4 \sum_{s=1}^S a_{q,s}$
$\bar{a}_s$	Mean size of spot $s$ over all quadrants	$\frac{1}{4} \sum_{q=1}^4 a_{q,s}$
$\bar{a}_q$	Mean size of spots in quadrant $q$	$\frac{1}{S} \sum_{s=1}^S a_{q,s}$
$\sigma(a)$	Standard deviation in spot size	$\left( \frac{1}{4S} \sum_{q=1}^4 \sum_{s=1}^S (a_{q,s} - \bar{a})^2 \right)^{1/2}$
$\sigma(a)_s$	Standard deviation in size of spot $s$ over all quadrants	$\left( \frac{1}{4} \sum_{q=1}^4 (a_{q,s} - \bar{a}_s)^2 \right)^{1/2}$
$\sigma(a)_q$	Standard deviation in size of spots in quadrant $q$	$\left( \frac{1}{S} \sum_{s=1}^S (a_{q,s} - \bar{a}_q)^2 \right)^{1/2}$
$\bar{c}_{vb}$	Mean coefficient of variation in spot size between quadrants	$\frac{1}{S} \sum_{s=1}^S \frac{\sigma(a)_s}{\bar{a}_s}$
$\bar{c}_{vw}$	Mean coefficient of variation in spot size within a quadrant	$\frac{1}{4} \sum_{q=1}^4 \frac{\sigma(a)_q}{\bar{a}_q}$
$(\bar{x}_s, \bar{y}_s)$	Mean coordinates of spot $s$	$\left( \frac{1}{4} \sum_{q=1}^4 x_{q,s}, \frac{1}{4} \sum_{q=1}^4 y_{q,s} \right)$
$\langle r \rangle$	Mean positional error	$\frac{1}{4S} \sum_{q=1}^4 \sum_{s=1}^S \left( (x_{q,s} - \bar{x}_s)^2 + (y_{q,s} - \bar{y}_s)^2 \right)^{1/2}$

is the intensity of the optical trapping beam. In our case, this is given by

$$I(r) = \frac{P_b \rho_1^2}{\pi w_0^2 \rho_N^2 J_1^2(\rho_N)} J_0^2\left(\frac{\rho_1 r}{w_0}\right), \quad (2)$$

where  $P_b$  is the total power in a single Bessel beam of the array,  $\rho_i$  is the location of the  $i^{\text{th}}$  zero of  $J_0(\rho)$ ,  $w_0$  is the radial location of the first zero of the Bessel beam, and  $N$  is the number of rings (including the central spot) in the truncated Bessel beam.

In order to predict the mean positional error, we assume a harmonic potential well within the central lobe of the Bessel beam, and calculate an effective spring constant for the trap

$$K = - \left. \frac{\partial F}{\partial r} \right|_{r=0} = \frac{2n_m R^3 \rho_1^4 P_b}{c w_0^4 \rho_N^2 J_1^2(\rho_N)} \left( \frac{m^2 - 1}{m^2 + 2} \right). \quad (3)$$

The probability of the center of the particle being in a differential annulus with radius  $r$  is then given by Boltzmann statistics

$$P(r) dr = A 2\pi r \exp\left(-\frac{Kr^2}{2kT}\right) dr, \quad (4)$$

where  $A$  is a normalization constant,  $k$  is Boltzmann's constant, and  $T$  is the temperature. The mean positional error is then given by

$$\langle r \rangle = \int_0^\infty r P(r) dr = \sqrt{\frac{\pi kT}{2K}}. \quad (5)$$

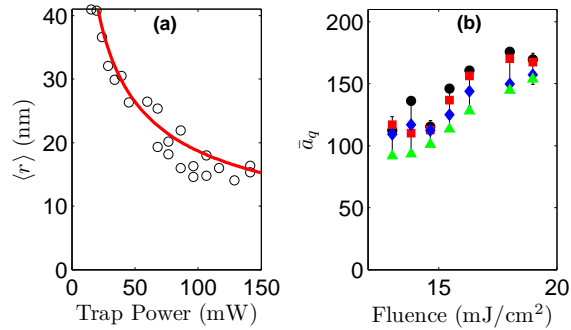


Fig. 3. (a) Relative positioning accuracy between quadrants as a function of individual beam power  $P_b$ . The circles are experimental, while the solid red line is the model prediction without any fitting parameters. (b) Spot size vs. incident fluence. The mean size in each quadrant  $\bar{a}_q$  is plotted for quadrants  $q = 1$  to 4 using black circles, red squares, blue diamonds, and green triangles, respectively. The full length of the vertical error bars is given by twice the standard deviation for all quadrants combined. For all points, the trapping power in each beam is 140 mW.

#### 4. Repeatability results & discussion

In Fig. 3(a),  $\langle r \rangle$  is plotted as a function of  $P_b$  for our parameters, alongside the experimental data. For this curve, the value of  $K/P_b$  is determined from Eq. 3 to be  $185 \text{ fN nm}^{-1} \text{ W}^{-1}$ . High trapping powers restrict Brownian motion, keeping the particles more securely in the trap and resulting in positioning accuracy better than 15 nm. Note the excellent parameter-free fit between the experiment and the Rayleigh trapping model. Due to limitations in the precision of the translation stage and environmental vibrations, absolute positioning accuracy tends to be several times larger. However, these effects do not represent a fundamental limit of the technique.

Methods to further improve positional accuracy can be found from equations 3 and 5. In addition to increasing the beam power, one can decrease the number of rings  $N$  in the Bessel beam, reduce  $w_0$ , increase the radius of the bead  $R$ , or reduce the temperature  $T$ . Of these options, reducing  $w_0$  is the most attractive due to the quadratic dependence in Eq. 5. Furthermore, reducing  $w_0$  has the least significant side effects of the available options. Decreasing the number of rings reduces the propagation length of the Bessel beam, requiring more precise longitudinal positioning accuracy. Increasing the size of the bead increases the spot size [16]. To get a significant benefit from lower temperatures, one would need to turn to cryogenic liquids, which would require more equipment and may not be compatible with all systems. The physical lower limit on  $w_0$  for our trapping laser wavelength is  $\lambda \rho_1 / (2\pi) = 407 \text{ nm}$ . Keeping the other parameters the same, this would improve positional accuracy by a factor of almost 7, leading to accuracies better than 3 nm.

The mean spot size is affected by both the incident fluence and the trapping power. The dependence on incident fluence is shown in Fig. 3(b), and has been previously discussed in detail [16]. At lower fluences, spot sizes are smaller because the width of the region below the bead that surpasses the material modification threshold fluence is narrower. By carefully adjusting the fluence, we are able to produce spots with mean radius over all four quadrants less than 110 nm. These spot sizes are highly repeatable, with coefficients of variation less than 15%.

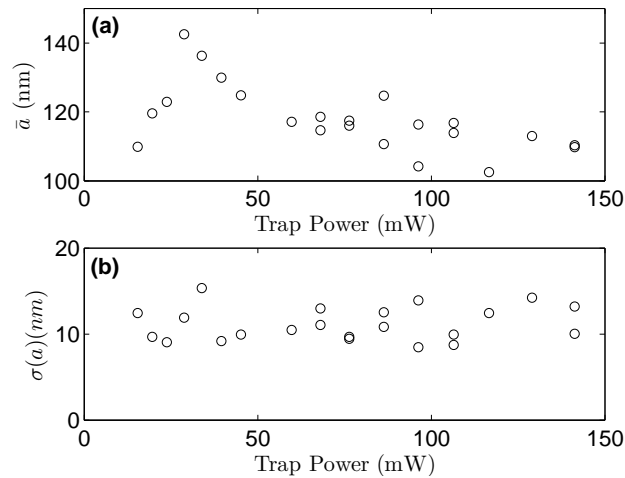


Fig. 4. Dependence of spot size on trapping power. (a) Mean spot size. (b) Standard deviation in spot size. A linear least-squares fit is plotted to illustrate the downward trend. All data is taken with an incident fluence of  $15 \text{ mJ/cm}^2$

The effect of trapping power on spot size for a fixed pulsed laser intensity is more subtle. In Fig. 4(a), the mean spot size reaches a maximum at a trapping power around 30 mW, and then decreases at higher trapping powers. This is a consequence of the decreasing separation between the bead and the surface as the trapping power increases. Larger trapping power leads to stronger radiation pressure which is balanced by the electrostatic double-layer repulsion at a smaller separation distance. Direct measurement and quantitative modeling of these forces in our system are being developed [27].

At low trap powers, the bead is kept several hundred nanometers away from the surface due to the electrostatic double-layer repulsion between the particle and substrate. At these separations, the intensity enhancement at the surface is relatively small. Therefore, the pulsed laser intensity is above threshold only near the peak enhancement, leading to a small spot size. As the trap power increases, the bead is pushed closer to the surface. The corresponding intensity enhancement increases and the same laser power will produce an increasingly larger spot. Eventually, one approaches a near-field focal length where the intensity enhancement reaches its global maximum.

At separations on the order of the focal length and smaller, it becomes difficult to predict the spot size without quantitative modeling. This is because of the non-Gaussian shape of the light field below the bead and because of two competing effects: (1) being closer to the focal length increases the fluence enhancement, increasing the size of the spot, and (2) being closer to the focal length implies a tighter confinement of the light, decreasing the size of the spot. FDTD modeling indicates that at low fluence, the spot size is greatest at an intermediate distance and smaller at very low and very large separations [16]. This qualitatively agrees with what is presented in Fig. 4(a).

Fig 4(b) shows the spot size is highly uniform with deviations less than 15 nm, and that this uniformity shows no clear dependence on trapping power. There are five potential sources of variability in feature size: Brownian motion, variations in bead size, power variations in the trapping laser, spatial fluence variations in the pulsed laser beam, and shot-to-shot energy variations in the pulsed laser. If Brownian motion in the longitudinal direction were the limiting

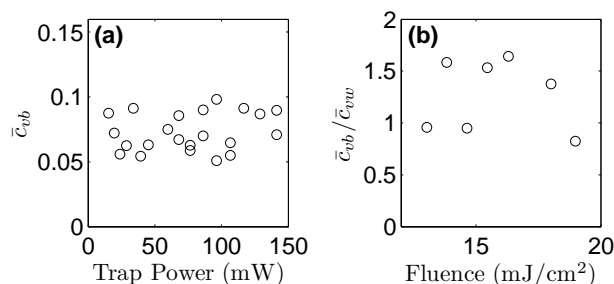


Fig. 5. Coefficients of variation in spot size. (a) Mean coefficient of variation between quadrants as a function of trapping power with an incident fluence of  $15 \text{ mJ/cm}^2$ . (b) Mean coefficient of variation between quadrants normalized by the coefficient within quadrants as a function of incident fluence with a trapping power of  $140 \text{ mW}$ .

factor in spot size uniformity,  $\sigma(a)$  would decrease with increasing trap power. Since this is not the case, Brownian motion does not limit the feature size uniformity in this study.

In order to identify which of the remaining four sources are the limiting factors, we compare the mean coefficient of variation in spot size *between* quadrants,  $\bar{c}_{vb}$ , to the mean coefficient of variation *within* quadrants,  $\bar{c}_{vw}$ , as shown in Fig. 5. Figure 5(a) shows that the variation in spot size between quadrants is less than 10% of the spot size and that there is no observable dependence on trapping power, thus implying that power variations in the trapping laser are not significant.

For the remaining three sources of uncertainty, we look to the ratio of  $\bar{c}_{vb}$  to  $\bar{c}_{vw}$ . If the bead size and/or spatial variations in the pulsed laser are dominant, the ratio should be greater than 1 because the variation between quadrants would be larger than the variation within a quadrant. Conversely, if the shot-to-shot pulse energy variations dominate, the ratio will become less than one. In Fig. 5(b), it can be seen that although the ratio shows no clear trend with respect to pulse laser energy, the ratio is for the most part greater than 1. This result, together with the fact that some quadrants tend to have a consistently lower mean spot size than others for a given experiment (see Fig. 3(b)) implies that variations in the pulsed laser fluence distribution and/or bead size have the greatest effect on spot size variability.

## 5. Conclusions

We have demonstrated that optical trap assisted nanolithography can be performed in a parallel fashion to generate an array of identical arbitrary patterns of both continuous and discrete nature. Comparing patterns written in parallel has allowed us to eliminate errors due to macroscopic mechanical vibrations and imprecisions in the translation stage in order to identify the fundamental limitations on the accuracy and repeatability of the technique. We have generated individual features with sizes less than  $\lambda/3$  and a relative positioning accuracy between patterns better than  $15 \text{ nm}$ . This positioning accuracy is primarily determined by Brownian motion and therefore higher trapping powers combined with a reduction in the size of the central lobe of the beam provide further improvements in positioning capability, with the potential for nanometer scale accuracy.

The uniformity in feature size is also better than  $15 \text{ nm}$ , where in this case, the limitation is due to laser spatial intensity distribution and/or dispersion in microsphere size. Ultimately Brownian motion represents a fundamental limit to size uniformity and since the experiment has not yet reached that limit, we expect significant improvements with continued development.

Nonetheless, we see this study as an important first step toward massively parallel direct-write nanolithography.

### Appendix: determining spot size and location

The general procedure for obtaining the locations and sizes for each spot is given immediately below, and a more detailed description follows.

1. Align the four quadrants in the image by finding the maxima of the cross-correlations between quadrants.
2. Create an overlay image by superimposing the four aligned quadrants.
3. Find the exact coordinates of each spot in the overlay image.
4. Find the size of each spot in each quadrant.
5. Find the exact coordinates of each spot in each quadrant, using the overlay spot locations as initial guesses.
6. Calculate statistical quantities based on spot size and location.

To begin aligning the four quadrants in an image, a background level is determined by finding the mean level in a region without any spots. This background is then subtracted from the entire image. The upper-left quadrant of the image is taken to be the reference quadrant, to which the other three quadrants will be aligned. The shift required to align each quadrant is determined by finding the location of the maximum of the 2D cross-correlation between the reference quadrant and each other quadrant. Overlay images such as those in Figs. 1(b) and (e) are produced by shifting the three non-reference quadrants (and cropping or padding with zeroes if necessary) and then summing all four quadrants.

The approximate radius of a single spot is determined by eye, and a sample Gaussian spot with this  $1/e$  radius is generated in a square region with a width four times that of the approximate radius. Let the size of this region be  $(2m + 1) \times (2m + 1)$  pixels, where  $m$  is an integer.

Next, an approximate location is determined by eye for each spot in the overlay image. A 2D cross-correlation between the sample Gaussian and a neighborhood  $N_s$  around each approximate spot location is performed. The true overlay location  $(x_s^o, y_s^o)$  for each spot  $s$  is determined by finding the location of the maximum of each cross-correlation.

These true overlay spot locations are then used as the approximate spot locations for each individual quadrant. Normalized Gaussians of varying width are cross-correlated with a neighborhood (also  $(2m + 1) \times (2m + 1)$ ) around each approximate spot location. The true spot size  $a_{q,s}$  of spot  $s$  in quadrant  $q$ , in pixels, is found to be the size of the Gaussian with whom the peak cross-correlation value is greatest. Formally, let the brightness of pixel  $(x, y)$  in quadrant  $q$  be given by  $Q_q(x, y)$ . Define the neighborhood for spot  $s$  to be:

$$N_s = \left\{ (x, y) \left| \begin{array}{l} |x - x_s^o| \leq m \\ |y - y_s^o| \leq m \end{array} \right. \right\}. \quad (6)$$

Then define the windowed brightness of each pixel as,

$$U_{q,s}(x, y) = \begin{cases} Q_q(x, y) & \text{for } (x, y) \in N_s \\ 0 & \text{otherwise} \end{cases}. \quad (7)$$

Then the size of each spot,  $a_{q,s}$ , is given by the value of  $\alpha$  which maximizes the quantity:

$$\max_{(x,y) \in N_s} \left( \sum_{i=-m}^m \sum_{j=-m}^m U_{q,s}(x+i, y+j) A(\alpha) e^{-\frac{i^2+j^2}{\alpha^2}} \right), \quad (8)$$

where

$$A(\alpha) = \left( \sum_{i=-m}^m \sum_{j=-m}^m \left( e^{-\frac{i^2+j^2}{\alpha^2}} \right)^2 \right)^{-1/2} \quad (9)$$

is a normalization constant. The center of the spot is given by the  $(x, y)$  location of the maximum of the cross-correlation in Eq. 8 for  $\alpha = a_{q,s}$ . We denote the location of spot  $s$  in quadrant  $q$  as  $(x_{q,s}, y_{q,s})$ . Finally, the location and size of each spot in each quadrant are visually verified to be correct.

Once the locations and sizes of all the spots are found, several statistical quantities are calculated to quantify pattern quality. In all of these calculations only the spots in the two largest “L’s” were used (see Figs. 1(d) and (e)); in the smallest “L” spots sometimes overlapped, and so these points were not considered. This results in  $S = 34$  useful spots in each quadrant. The statistical quantities calculated are summarized in Table 1.

### Acknowledgments

We wish to thank James Joy for help in acquiring SEM images and the development of some lab automation utilities and Timo Nieminen for discussions regarding our adaptation of his code to deal with Mie trapping forces from a Bessel beam. We also wish to thank the Air Force Office of Scientific Research for financial support.